electronics

MDPI

Article

Implantable and Degradable Wireless Passive Protein-Based Tactile Sensor for Intracranial Dynamic Pressure Detection

Wanjing Li †, Andeng Liu †, Yimeng Wang †, Kui Qu, Hao Wen, Jizhong Zhao, Yating Shi, Hao Wang, Meidan Ye and Wenxi Guo *

Department of Physics, College of Physical Science and Technology, Research Institution for Biomimetics and Soft Matter, Xiamen University, Xiamen 361005, China; wanjingli@stu.xmu.edu.cn (W.L.); andengliu@stu.xmu.edu.cn (A.L.); 19820201153614@stu.xmu.edu.cn (Y.W.); 19820201153570@stu.xmu.edu.cn (K.Q.); 19820191152999@stu.xmu.edu.cn (H.W.); 19820180155648@stu.xmu.edu.cn (J.Z.); 19820180155642@stu.xmu.edu.cn (Y.S.); h_wang@xmu.edu.cn (H.W.); mdye@xmu.edu.cn (M.Y.)

* Correspondence: wxguo@xmu.edu.cn

† These authors contributed equally to this work.

Abstract: Implantable sensors normally require devices with excellent biocompatibility and flexibility as well as wireless communication. Silk fibroin (SF) is an ideal material for implantable electronic devices due to its natural biodegradability and biocompatibility. In this work, we prepared SF protein materials with different force/chemical properties through mesoscopic regulation, and realized full protein replacement from substrate to dielectric elastomer for implantable sensors, so as to achieve controlled complete degradation. In wireless tests simulating intracranial pressure, the SF-based all-protein sensor achieved a sensitivity up to 4.44 MHz/mmHg in the pressure range of 0–20 mmHg. In addition, the sensor is insensitive to temperature changes and tissue environments, and can work stably in simulated body fluids for a long time. This work provides a wireless passive, all-protein material solution for implantable pressure sensors.

Keywords: silk fibroin; implantable; degradable; biocompatibility; wireless passive; pressure sensor

check for updates

Citation: Li, W.; Liu, A.; Wang, Y.; Qu, K.; Wen, H.; Zhao, J.; Shi, Y.; Wang, H.; Ye, M.; Guo, W. Implantable and Degradable Wireless Passive Protein-Based Tactile Sensor for Intracranial Dynamic Pressure Detection. *Electronics* **2023**, *12*, 2466. https://doi.org/10.3390/electronics12112466

Academic Editors: J.-C. Chiao and Jianjun Luo

Received: 29 April 2023
Revised: 21 May 2023
Accepted: 22 May 2023
Published: 30 May 2023

1. Introduction

Implantable bioelectronics have made tremendous progress in the past decades. The future trend of implantable bioelectronics will shift to having multifunctional, flexible, miniaturized, wireless, and biodegradable micro/nano systems [1]. In addition, implantable devices require a high level of material biocompatibility. Among implantable bioelectronic devices, implantable sensors can monitor various physiological indicators of the human body, such as pH [2], oxygen [3], body temperature [4], glucose [5], pressure, and so on. Among them, implantable pressure sensors can monitor pressure in various parts of the body depending on the designed sensor structure, such as intraocular pressure [6,7], blood pressure [8,9], abdominal pressure [10], bladder pressure [11], intracranial pressure [12–17], etc. Intracranial pressure is a crucial diagnostic parameter for monitoring various types of severe brain injury diseases. Traumatic brain injury (TBI) is a major health and socioeconomic problem worldwide [18]. TBI raises intracranial pressure by 5–10 mmHg, which may block blood flow leading to fatal ischemia and requires immediate treatment [19]. Elevated intracranial pressure is also a key pathological symptom leading to secondary brain injury. Therefore, monitoring of intracranial pressure is essential for brain patients [20].

Existing implantable commercial sensors have been called the gold standard for intracranial pressure monitoring due to the accuracy of monitoring [21], but they are usually connected via a wired connection and require an external power supply, which limits the patient's range of motion and has risks such as battery heating and failure. Therefore, researchers have prepared LC wireless passive pressure sensors for intracranial pressure monitoring. For example, Bao et al. prepared ultra-small size LC pressure sensors with a sandwich structure, using flexible polyimide as the substrate and microcone styrene-butadiene-styrene (SBS) as the dielectric layer. Its sensitivity was ≈ 1.084 MHz/mmHg, which can continuously monitor intracranial pressure values in mice models in real time and also human pulse signals [13]. Commercial sensors and some existing implantable wireless passive pressure sensors are made of non-degradable materials [12–17] and require surgical removal after patient recovery. Long-term implantation and secondary surgery both carry risks such as infection. In recent years, many researchers have prepared degradable materials for implantable devices. For example, Rogers et al. prepared bioresorbable wireless passive pressure sensors for monitoring intracranial pressure with a sensitivity of ≈200 kHz/mmHg and a resolution as low as 1 mmHg. When the sensor was implanted in a mice model, it exhibited stable operation for 4 days [19]. Silk (SF), a natural protein material derived from silk fibers, has excellent mechanical properties, biocompatibility, and biodegradability [22–25] and is well suited as a device material for implantation in vivo. However, inherent brittleness and chemical instability of pure SF limits its application in flexible electronic devices.

In this work, we modulate the internal structure of the material from the nanoscale to the mesoscale, i.e., mesoscopic modulation, and prepare SF protein materials with different stress/chemical properties to achieve an all-protein substitution of the implantable sensor from the substrate to the dielectric elastomer, thus achieving the key technical specification of controlled degradation. We prepared a flexible all-protein implantable wireless passive pressure sensor. It has a top-down seven-layer structure assembled as shown in Figure 1d. The mechanical properties and stability of natural silk protein materials are poor, and the SFPF (encapsulation layer, substrate) with good flexibility and stability and the SFE (dielectric layer) with low modulus and high elasticity were prepared using mesoscopically regulated silk protein; the water-soluble magnesium metal wire with good biocompatibility was used for the electrode. The whole sensor has good biocompatibility and controlled degradability. It has a novel compact LC structure, which allows the device to have high space utilization. The sensitivity of the device is increased to 4.44 MHz/mmHg in the pressure range of 0–20 mmHg. The sensitivity of the device was 4.46 MHz/mmHg even under porcine skin cover. Meanwhile, in vitro simulation experiments showed that the sensor was insensitive to temperature changes and tissue environmentd and could operate stably in simulated body fluids for 36 h. This work provides a wireless passive all-protein material solution for implantable pressure sensors.

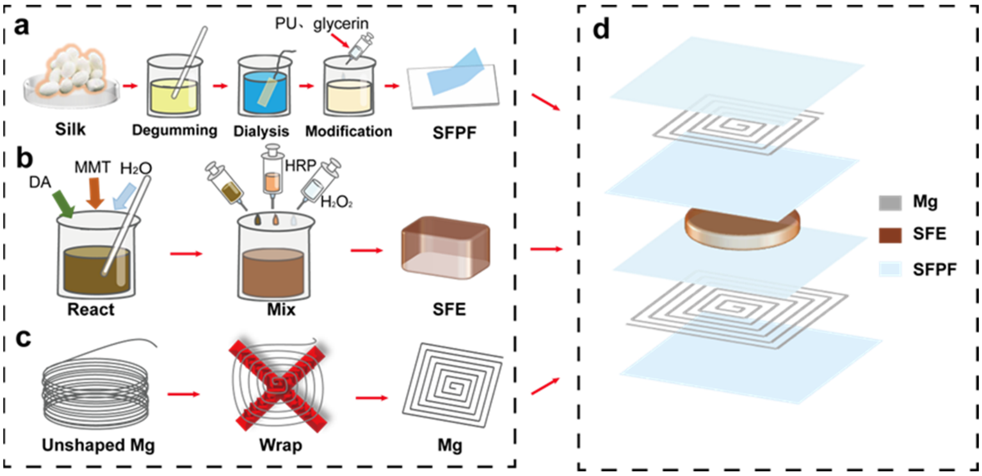

Figure 1. Flow chart of sensor preparation. (**a**) Flow chart of SFPF preparation. (**b**) Flow chart of SFE preparation. (**c**) Flow chart of inductor coil preparation. (**d**) Sensor structure diagram.

2. Materials and Methods

2.1. Materials

All chemical reagents were in analytical grade and used as received without further treatment. Glycerol, ethyl alcohol, and sodium carbonate (Na_2CO_3) were purchased from Sinopharm Chemical Reagent Co., Ltd. (Shanghai, China). Polyurethane (PU) was obtained from EZ Brush Corporation (Qingdao, China). Lithium bromide (LiBr) was purchased from Aladdin Industrial Corporation (Shanghai, China). Bombyx mori silkworm cocoons were bought from Guangxi Sericulture Technology Co., Ltd. (Liuzhou, China). Horseradish peroxidase (HRP) was purchased from Shanghai Jiji Biochemical Technology Co. (Shanghai, China). Hydrogen peroxide was purchased from Shanghai Moen Chemical Technology Co. (Shanghai, China). Montmorillonite powder was purchased from Shanghai JiZhi Biochemical Technology Co., Ltd. (Shanghai, China). Dopamine hydrochloride was purchased from Beijing Solabao Technology Co. (Beijing, China). Magnesium wire was purchased from Hi-Tech New Material Technology Co. (Beijing, China). The biological tissue glue was purchased from Beijing Yoshida Biotechnology Co. (Beijing, China).

2.2. Preparation of SF Solution

The SF solution was prepared according to our previous method. First, 20 g of silk cocoon shells were boiled in 2 L of deionized water with 15 g of Na_2CO_3 for 30 min, rinsed with deionized water and this was repeated twice. Then, the washed silk protein was dried in an oven at 60 °C for 6 h; the dried silk protein was dissolved in 9.5 mol/L lithium bromide solution at 60 °C. The completely dissolved silk protein solution was dialyzed in deionized water using cellulose tubing (cut-off molecular weight of 3500 Da) for 3 days, and the deionized water was changed every 4 h. The regenerated SF solution was prepared and its concentration was 4–5%.

2.3. Preparation of SFPF and SFE

The preparation of silk fibroin composite film (SFPF) and hydrogel elastomer (SFE) requires the extraction of silk fibroin (SF) protein materials from silk fibers, which includes degluing, dissolution, dialysis, centrifugation, and molding (Figure 1). The solution method is used to prepare SFPF to facilitate the meso-doping of SF material regeneration. Here, we used the previously reported polyurethane (PU) and glycerin doping method to prepare SFPF with good flexibility, good water resistance, and certain high temperature resistance as the substrate and encapsulation layer of the device, so as to prevent liquid penetration and affect the stability of electrodes and wireless signals. Polyurethane and glycerol (0.1 drop/mL) were added to the regenerated silk solution, with PU accounting for 4% of the mixture. The mixed solution was injected into a Petri dish at 27 °C and 50% relative humidity to obtain about 25 µm thick SFPF.

In Figure 1b, highly elastic SFE was prepared by adding horseradish peroxidase (HRP) and hydrogen peroxide (H_2O_2) to the regenerated silk solution, followed by a mixture of dopamine hydrochloride (DA), montmorillonite (MMT), and deionized water. 1 mg of dopamine hydrochloride powder and 15 mg of montmorillonite powder were added to 2 mL of deionized water and stirred for 3 h at room temperature with a magnetic stirrer at 500 r. Next, 1000 µL of the mixture was added to 7 mL of regenerated silk solution, and then 500 µL of HRP solution (10,000 U mL^{-1}) and 100 µL of H_2O_2 solution. After mixing well, the mixture was poured into a Petri dish and then put into a constant temperature and humidity chamber at 35 °C. After 5 h, the SFE was removed and obtained.

2.4. Preparation of Electrode Layers

The 3D-printed molds of different sizes (1.5 cm × 1.5 cm and 2 cm × 2 cm in size, respectively) with 1 mm pitch between mold notches were used, and 5 turns of square coils of different sizes were wound with magnesium wire of 300 µm in diameter, which were used as upper and lower spiral induction coils (Figure 1c). Next, 20 V/V% acetic acid was used to remove the surface oxide layer, and then the electrodes were transferred to the SFPF.

2.5. Fabrication of SF Wireless Pressure Sensors

The prepared parts of the material were assembled into the sensor. The structure diagram is shown in Figure 1d. From top to bottom, the SF wireless pressure sensor consists of a combination of seven layers: upper encapsulation layer, upper electrode, upper substrate, dielectric layer, lower substrate, lower electrode, and lower encapsulation layer. The upper and lower encapsulation layers and substrate are composed of SF composite film, the upper and lower electrodes are wound magnesium wires, and the dielectric layer is a soft SF elastomer. The two magnesium coils are fixed to the SFPF by applying an appropriate amount of bio-glue, and the sealing machine will be used around the encapsulation layer (assisted by commercially available biocompatible tissue glue).

2.6. Characterization

As shown in Figure 2a, SFPF demonstrates high transparency (>90%) in visible light from 400 to 800 cm^{-1}. In addition, SFPF had better malleability (240%) compared to pure SF (Figure 2b). The cross-sectional scanning electron microscopy image of SFE showed a porous structure (Figure 2d). Such a structure promoted the hydrogel to have good compression resistance (>60%), as shown in Figure 2e. The modified regenerated silk protein elastomer has good elasticity as shown in the 100 times compression stress–strain curve (Figure S1, Supplementary Materials). The modified silk protein elastomer has better curve recombination compared with pure silk protein elastomer, indicating that the modified elastomer has good resilience and stability, and the modified elastomer has a lower modulus. The tensile stress–strain properties of the pure SF film, SFPF membranes, and SFE were tested using a micro tensile tester (Instron 5948, Instron, High Wycombe, UK). The transmittance of the SFPF membranes was measured at a range of 400 nm to 2000 nm by a UV-Vis-NIR spectrophotometer (Lambda 750, Lambda, Singapore). The morphology of the SFE was obtained using scanning electron microscopy (Σ-HD, Karl Zeiss, 5 KV, ZEISS Sigma, Baden-Württemberg, Germany), which required the SFE to undergo a freeze-drying process. The S11 signal and resonant frequency were examined using a vector network analyzer. The temperature distribution images were obtained from a thermal imager (Fluke TiS40, Fluke, Everett, WA, USA).

2.7. Biocompatibility and Degradation Evaluation

The mouse preosteoblast cell line MC3T3-E1 (Cell Resource Center, Beijing, China) was maintained in minimal essential medium alpha medium (alpha-MEM, HyClone) supplemented with 10 volumes of fetal bovine serum and 1 volume of the antibiotic penicillin–streptomycin in a CO_2 incubator. At approximately 80% confluence, cells were harvested and cultured on sterilized samples. Samples were kept in 24-well culture plates seeded at a density of 2×10^4 cells/well. After 1, 3, and 7 days of culture, cells were stained with Calcein-AM (Sigma, Cibolo, TX, USA) and observed under a fluorescent microscope. The SFPF and SFE were completely immersed in a solution of papain at a concentration of 10% at room temperature until the SFPF and SFE were completely degraded and disappeared.

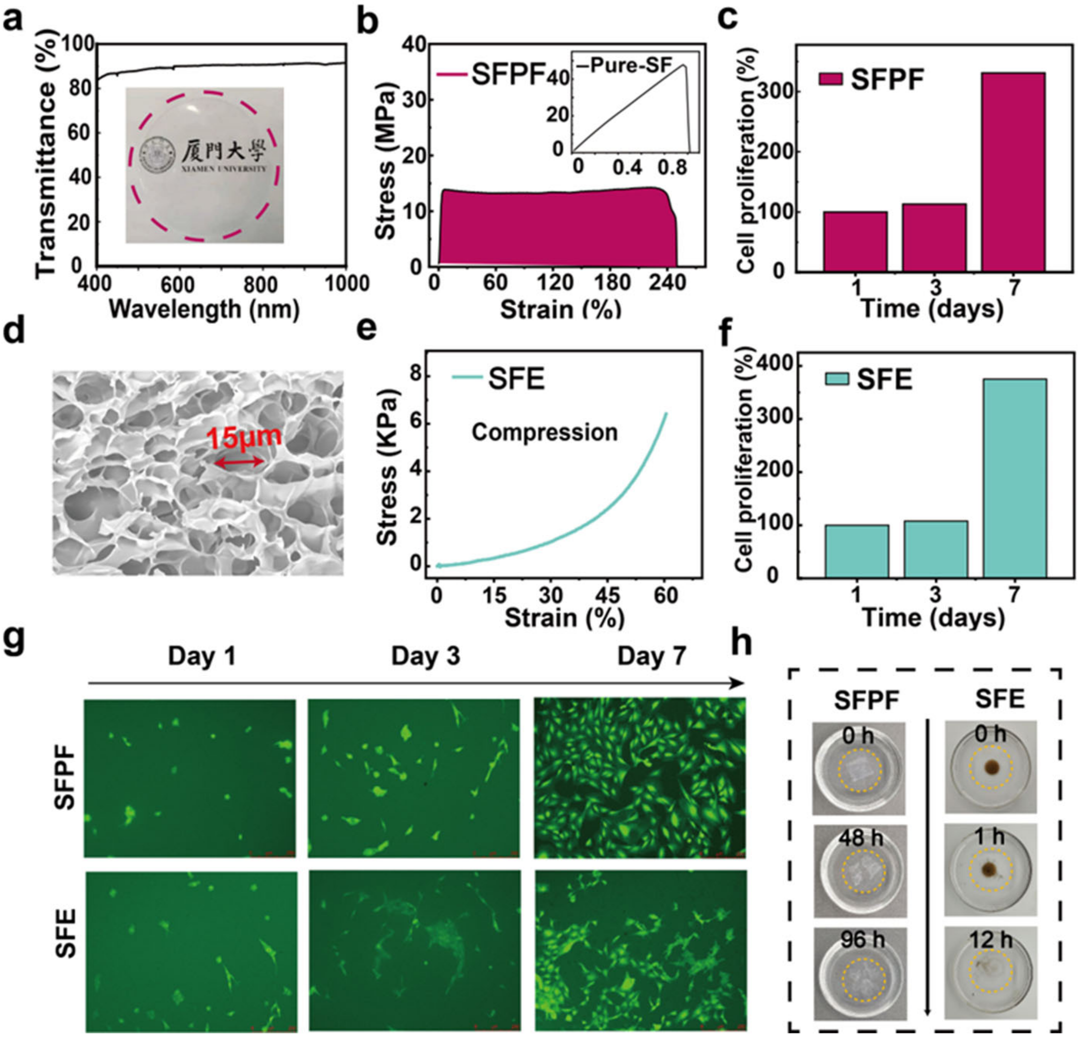

Figure 2. Characterization of SFPF and SFE. (**a**) Light transmission and optical photographs of SFPF. (**b**) Tensile test of SFPF, inset is a graph of tensile test of pure SF film. (**c**) Plot of proliferation data of cells cultured on SFPF over one week. (**d**) SEM image of SFE. (**e**) Compression properties of SFE at 60% strain. (**f**) Plot of proliferation data of cells cultured on SFE over one week. (**g**) Immunofluorescence images of cells cultured on SFPF and SFE over one week. Scale bar: 250 µm. (**h**) Optical images of gradual degradation of SFPF and SFE under 10% papain.

3. Results and Discussion

3.1. Biocompatibility and Degradability

Biodegradability and biocompatibility are important for implantable electronic devices. To investigate the biocompatibility of SFPF and SFE, we prepared SFPF with a diameter of 1 cm and a thickness of 50 µm and a cylindrical SFE with a diameter of 1 cm and a height of 1 mm for the cell proliferation test. The proliferation of mouse osteoblast precursor MC3T3-E1 cells cultured on SFPF and SFE within one week was evaluated using the CCK-8 assay. According to Figure 2c,f, it can be seen that the cell count increased with the increasing number of days for both SFPF and SFE. The cell count on the seventh day was significantly higher than that on the first and third days. To further observe the attachment, proliferation, and morphology of cells on SFPF and SFE, the cells were fluorescently stained as shown in Figure 2g. The fluorescence staining showed that on the first day, the attached cells were shuttle-shaped and showed a filamentous stretching morphology and the cells were healthy. As the number of days increased, clusters of cells with a more diffuse cell morphology appeared, and the cell density was increasing, indicating that the cells were proliferating and growing. These indicate that both SFPF and SFE have good biocompatibility and non-toxicity to ensure the biosafety of the implanted devices.

Figure 2h shows the degradation of SFPF and SFE in 10% papain solution. SFPF was broken into many small fragments after 48 h immersion, and the fragments were further broken down after 96 h, while SFE was completely degraded at 12 h. These results confirm the degradability of SFPF and SFE. It is worth mentioning that the material used for the inductor coils—magnesium wire—is a recognized metal with good biocompatibility and easy hydrolysis ($Mg + 2\ H_2O \rightarrow Mg(OH)_2 + H_2$), which ensures the biocompatibility and degradability of the whole device.

3.2. Structural Design and Principle of the Sensor

The device structure is a typical sandwich structure. SFPF is used as the substrate and encapsulation layer. SFE is used as the dielectric layer. The device structure is shown in Figure 1d. The entire device is soft with a size of 2 cm × 2 cm × 5 mm so that only a small incision in the scalp is required, making it less invasive and easier to implant. As shown in Figure 3a, the device adopts a highly integrated compact asymmetric LC structure and replaces both the upper and lower pole plates of the parallel plate capacitor with inductor coils so that the spiral coil acts as inductor, capacitor pole plate, and antenna at the same time. The upper and lower coils do not need to be wired, and the connection is created by electromagnetic coupling. The quality factor of the sensor is high with such a structure (Figure 1d). This structure was tested in vitro with an S11 signal strength of −30.73 dB, and under a pig skin cover (simulation of implantation in human body), the S11 signal was able to reach −18.42 dB (Figure S2, Supplementary Materials). The defining equation of quality factor Equation (1) is as follows:

$$Q = \frac{1}{R}\sqrt{\frac{L}{C}} \tag{1}$$

where R is the resistance, L is the inductance, and C is the capacitance. To increase Q, C and R can be reduced or L increased as much as possible. The device adopts a dual coil structure to increase the inductance value. In fact, the equivalent circuit of the sensor includes both the parallel plate capacitance of the upper and lower double coils and the parasitic capacitance of the upper and lower coils, but the parasitic capacitance is much smaller than the parallel plate capacitance, so it is not considered. The specific sensing principle is that under pressure, the spacing d between the two coils above and below the sensor decreases, and the outer diameter of the flat spiral coil increases. The determinant of parallel plate capacitance is Equation (2):

$$\mathrm{C} = \frac{\varepsilon_r \mathrm{S}}{4\pi k d} \tag{2}$$

where ε_r is the dielectric constant of the hydrogel elastomer, S is the relative area of the polar plates, k is the electrostatic force constant, and d is the spacing between the two polar plates. The determinant of rectangular planar spiral inductance is shown in Equation (3):

$$\mathrm{L} = \mathrm{K}_1 \mu \frac{N^2 d_{avg}}{1 + K_2 \rho} \tag{3}$$

where N is the number of turns of the coil, μ is the permeability, and K_1 and K_2 are related to the layout and can be taken as 2.34 and 2.75. The average diameter is calculated in Equation (4):

$$\mathrm{d_{avg}} = \frac{(d_{in} + d_{out})}{2} \tag{4}$$

where d_{in} is the inner diameter and d_{out} is the outer diameter. The filling rate is calculated in Equation (5):

$$\rho = \frac{(d_{out} - d_{in})}{(d_{in} + d_{out})} \tag{5}$$

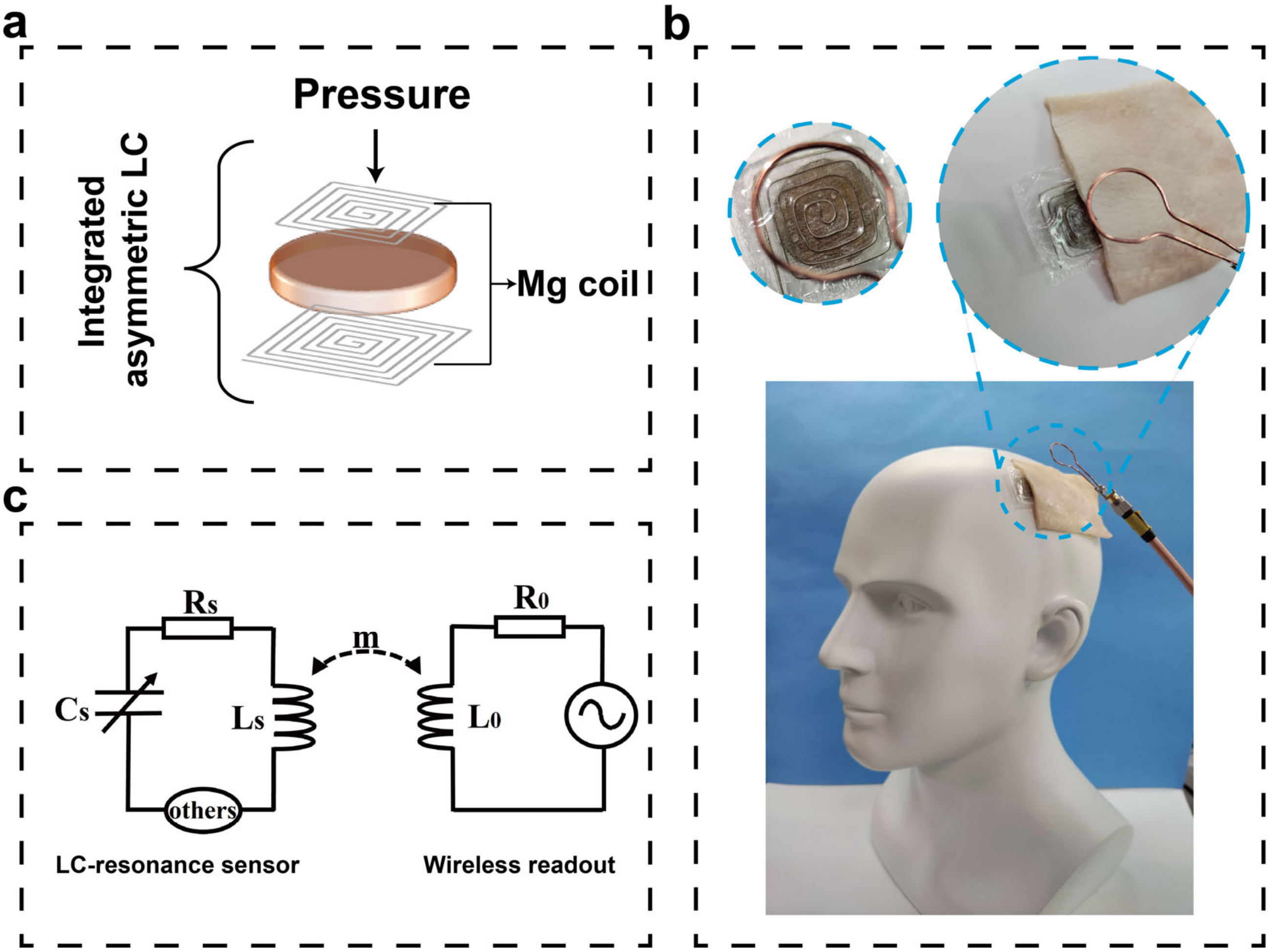

Figure 3. Schematic diagram of a flexible LC wireless passive pressure sensor, application scenario diagram and equivalent circuit diagram for wireless sensing. (**a**) Schematic diagram of an LC sensor with an integrated asymmetric structure, illustrated with a vertical inductive coil applying pressure. (**b**) Application scenario diagram of LC pressure sensor for intracranial pressure monitoring, inset shows a partial enlarged view and a top view of the device. (**c**) Equivalent circuit diagram of the pressure sensor and wireless readout system.

It is known that both capacitance and inductance of the resonant system increase (ignoring parasitic capacitance). The resonant frequency definition equation is Equation (6):

$$f = \frac{1}{2\pi\sqrt{LC}} \tag{6}$$

It is known that circuit resonant frequency which is monitored by the wireless coupling of the readout coil of the vector network analyzer decreases. The sensor is based on the principle of inductive coupling. The transmitting coil of the vector network analyzer generates a changing magnetic field that will excite the sensor, and the analyzer then outputs the resonant frequency signal of the sensor, making the device realize wireless passive sensing. The equivalent circuit diagram is shown in Figure 3c. Figure 3b shows a scenario diagram of the application of this sensor for intracranial pressure monitoring, and the inset shows a partial enlargement. The frequency variation with pressure has been pre-calibrated, and the pressure variation curve with time can be obtained from the frequency variation curve with time, thus enabling real-time dynamic pressure monitoring (Figure S3, Supplementary Materials).

3.3. LC Pressure Sensor Output Characteristics

The measurements show that the device provides a sensitivity of up to 4.44 MHz/mmHg over a pressure range of 0–20 mmHg, as shown in the calibration curve in Figure 4a. To simulate in vivo sensing, a 6 mm section of pigskin is spaced between the device and the detection antenna. The sensitivity of the device is not affected even with the pigskin covering up to 4.46 MHz/mmHg, as shown in Figure 4d. In the pressure range of 20–80 mmHg, the sensitivity of the device decreases to 0.89 MHz/mmHg (0.54 MHz/mmHg under the pigskin) due to reduced compressibility of the elastomer. In medicine, exceeding the normal intracranial pressure range (5 to 15 mmHg) requires immediate medical intervention. It is worth noting that this range coincides with the highly sensitive pressure monitoring range of our device. In addition, the device can monitor pressures from 0 to 150 mmHg. Figure 4b,e shows the measurement spectra at different pressures, showing that the device has a stable response to different pressures with and without pigskin. The sensor still has a clear S11 values even under the pigskin. The resonant frequency of the sensor decreases continuously under increasing pressure. The specific resonant frequency values and S11 values with pressure are shown in Tables S1 and S2. Figure 4c shows the measured spectrum of the device at different reading distances. The reading distance here is the distance between the reading coil and the top surface of the device (the reading coil is directly above the device). It can be seen that the farther the distance, the weaker the S11 signal. The maximum test distance can reach 13 mm. Figure 4f shows the variation of S11 intensity with the distance between the device and the reading coil under the pigskin. The reading distance at this point is the distance between the reading coil and the upper surface of the pigskin (the reading coil is directly above the device). It can be seen that the maximum readout distance is 7 mm under the pigskin cover. The variation tendency of S11 is consistent with those without the pigskin cover, indicating that the device operates independently of the pigskin and has the feasibility of being implanted into the organism. The specific S11 values with reading distance are shown in Tables S3 and S4. In addition to being implantable to monitor pressure in the body, the device can also be used as an electronic skin to wirelessly detect the motion of human joint movements. For example, the device can respond to finger flexion from 0° to 90°, with or without pigskin coverage to detect changes in frequency with pressure, the larger the bending angle, the smaller the resonant frequency (Figure S4, Supplementary Materials). In addition, considering the thermal effect of the induced current, the heat generation during the operation of the sensor implanted in the body was simulated and tested. The temperature change of the sensor was measured before and after one hour of operation (Figure S5, Supplementary Materials). It can be seen that the temperature of the device basically did not change (from 25.2 °C to 25.0 °C), indicating that the Joules of heat generated by the device is small and does not cause burning and discomfort when implanted in the body.

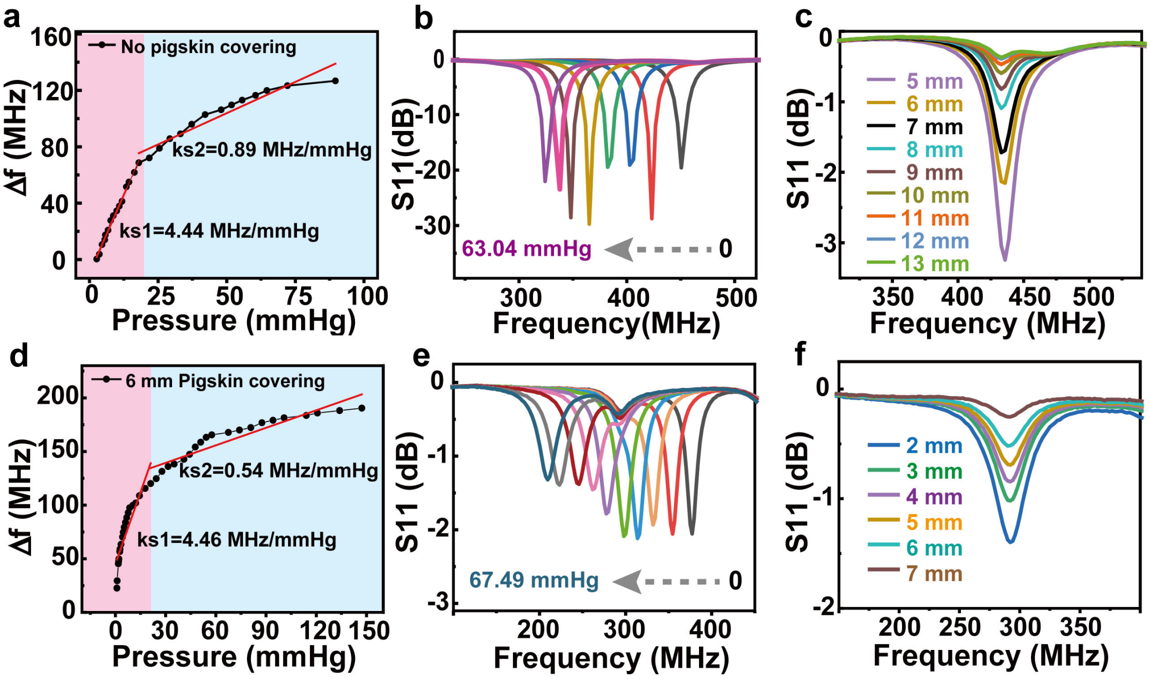

Figure 4. Output characteristics of the LC wireless passive pressure sensor without (**a**–**c**) and with pigskin coverage (**d**–**f**). (**a**,**d**) Sensitivity of the sensor. (**b**,**e**) Measurement spectra at different pressures. (**c**,**f**) The measured spectrum of the device at different reading distances.

3.4. In Vitro Simulation Experiments

To test the response of the pressure sensor over a wide range of pressures, we constructed a measurement device using a gas pressure chamber with the sensor glued to the side wall of the gas pressure chamber and a N_2 gas pump to apply different pressures to the sensor relative to atmospheric pressure. Next, 60 mM salt water is added to the pressure chamber to submerge the sensor to simulate the human intracranial environment, so the sensor is subjected to a pressure that is the sum of variable air pressure and fixed hydraulic pressure. In addition, an external barometer (XINSTER digital pressure gauge) is connected to the gas pressure chamber, which allows real-time monitoring of the air pressure value inside the gas pressure chamber. Similarly, the network analyzer is used in combination with a 20 mm diameter hand-wound single coil antenna used as a wireless reader, which is fixed to the outside wall of the pressure chamber and used to detect changes in resonant frequency. To better simulate the human tissue environment, the pressure chamber was temperature-controlled using a heat table (temperature range of 36–42 °C with a gradient of 2 °C). As in Figure 5a, the initial resonant frequencies of the sensors were measured at four temperatures. The results showed that the initial resonant frequencies of the devices remained the same at the four temperatures, indicating that the temperature had no effect on the initial resonant frequencies. This can ensure that the resonant frequency change of the device is caused by the pressure change. The sensitivity of the sensor at the 4 temperatures does not differ significantly, with an average sensitivity of 0.106 MHz/mmHg, and the detectable pressure range is 0–130 mmHg (Figure 5b). Figure 5c shows the measured spectrum of the device at 36 °C with different pressures. The device has a stable response at different pressures, and the resonant frequency decreases as the pressure increases. The device was immersed in salt water for 36 h. The resonant frequency remained unchanged, showing insensitivity to the tissue environment, which could ensure stable operation of the device in vivo for 36 h. After the 37th hour, the resonant frequency of the device slightly decreased, presumably due to the infiltration of salt water into the device, which causes an increase in capacitance (Figure 5d). The time for stable operation of the device is shorter than the time for the encapsulation layer to start degrading (in the degradation experiments, the degradation of the silk protein film started at the 48th hour), which ensures that the device will degrade after it has finished working. In conclusion, we prepared a pressure sensor with high pressure sensitivity and low temperature sensitivity.

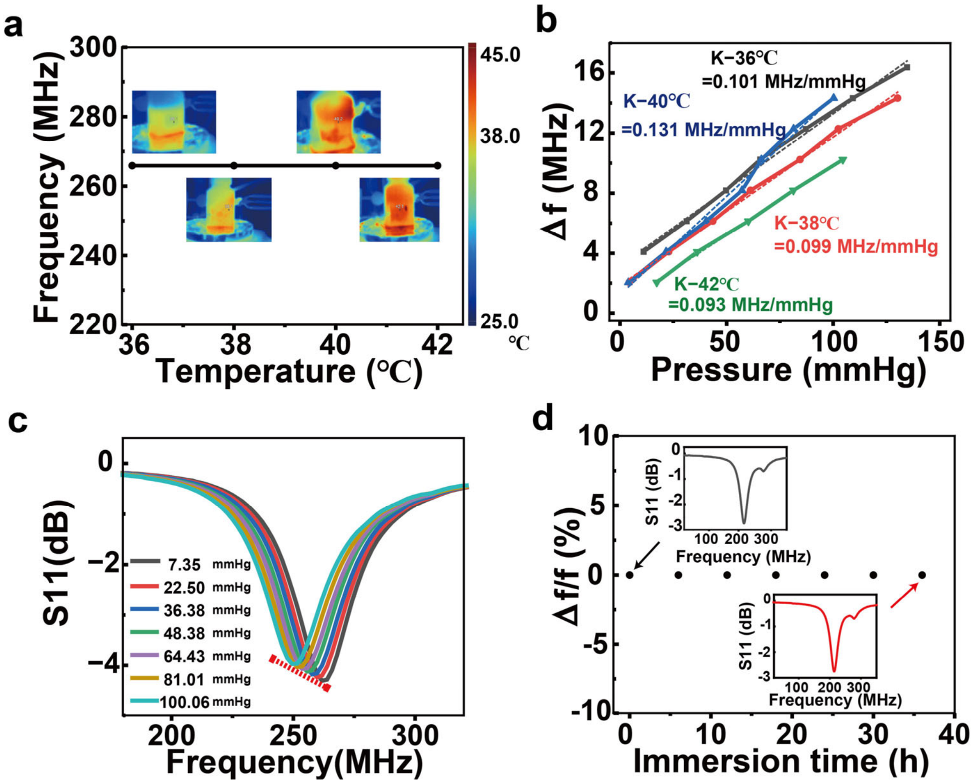

Figure 5. In vitro simulation experiments. (**a**) Initial resonant frequency of the sensor at different temperatures. (**b**) Sensitivity magnitude of the sensor at different temperatures. (**c**) The measurement spectrum of the sensor at different pressures at 36 °C. (**d**) The rate of change of the initial resonant frequency of the sensor versus the submersion time in salt water, where the insets show the measured spectrum of the sensor at 0 h and 36 h, respectively.

4. Conclusions

In conclusion, we report on a flexible implantable all-silk protein wireless passive LC pressure sensor with simple compact asymmetric structure, good biocompatibility, and controlled degradability. The sensitivity of the sensor reaches 4.44 MHz/mmHg in the range of 0–20 mmHg and remains high under the pigskin coating. The maximum reading distance of the device is 13 mm. In vitro simulation experiments show that the sensor has the potential to be implanted in vivo for real-time monitoring of dynamic pressure. The structure of the device can be further designed as a non-compact structure, that is, the inductive element and the capacitor element are separated. This is expected to increase the implantation depth so it can be applied to abdominal pressure, bladder pressure, and vascular pressure.

Supplementary Materials: The following supporting information can be downloaded at https://www.mdpi.com/article/10.3390/electronics12112466/s1, Figure S1: Comparison of cyclic compression tests of pure and modified regenerated silk hydrogel elastomers; Figure S2: Measurement spectrogram of the device when no pressure is applied in vivo and in vitro; Figure S3: Signal conversion flow diagram; Figure S4: Response of the sensor to 0–90° bending of the finger (a) without pigskin coverage, (b) with pigskin coverage; Figure S5: Thermograms before and after one hour of sensor operation, (a) before one hour, (b) after one hour; Table S1: Resonant frequency and return loss values (S11) of the device without pigskin cover under different pressures; Table S2: Resonant frequency and return loss values (S11) of devices with pigskin cover under different pressures; Table

S3: Return loss values (S11) of devices without pigskin coverage at different reading distances; Table S4: Return loss values (S11) of devices with pigskin coverage at different reading distances.

Author Contributions: Conceptualization, W.G.; methodology, W.L. and H.W. (Hao Wang); software, H.W. (Hao Wen) and W.L.; formal analysis, A.L. and W.L.; investigation, A.L., J.Z., W.L. and Y.S.; resources, Y.W. and K.Q.; writing—original draft, W.L.; writing—review and editing, W.G.; supervision, M.Y. and W.G.; project administration, W.G. All authors have read and agreed to the published version of the manuscript.

Funding: This work was supported by the National Nature Science Foundation of China (22175146, 52001265), Key research and development project of Jiangxi province (20212BBG73007), the Guangdong Natural Science Foundation (2021A1515010680), the Fundamental Research Funds for the Central Universities of China (20720210027, 20720222004), the "111" Project (B16029).

Data Availability Statement: All of the data created in this study are presented in the context of this article.

Conflicts of Interest: The authors declare no conflict of interest.

References

1. Sheng, H.; Zhang, X.; Liang, J.; Shao, M.; Xie, E.; Yu, C.; Lan, W. Recent Advances of Energy Solutions for Implantable Bioelectronics. *Adv. Healthc. Mater.* **2021**, *10*, 2100199. [CrossRef] [PubMed]
2. Cao, H.; Landge, V.; Tata, U.; Seo, Y.-S.; Rao, S.; Tang, S.-J.; Tibbals, H.F.; Spechler, S.; Chiao, J.C. An Implantable, Batteryless, and Wireless Capsule With Integrated Impedance and pH Sensors for Gastroesophageal Reflux Monitoring. *IEEE Trans. Biomed. Eng.* **2012**, *59*, 3131–3139. [CrossRef] [PubMed]
3. Rivas, L.; Dulay, S.; Miserere, S.; Pla, L.; Marin, S.B.; Parra, J.; Eixarch, E.; Gratacos, E.; Illa, M.; Mir, M.; et al. Micro-needle implantable electrochemical oxygen sensor: Ex-vivo and in-vivo studies. *Biosens. Bioelectron.* **2020**, *153*, 112028. [CrossRef] [PubMed]
4. Lu, D.; Yan, Y.; Avila, R.; Kandela, I.; Stepien, I.; Seo, M.H.; Bai, W.B.; Yang, Q.S.; Li, C.H.; Haney, C.R.; et al. Bioresorbable, Wireless, Passive Sensors as Temporary Implants for Monitoring Regional Body Temperature. *Adv. Healthc. Mater.* **2020**, *9*, 2000942. [CrossRef] [PubMed]
5. Lei, M.; Baldi, A.; Nuxoll, E.; Siegel, R.A.; Ziaie, B. A Hydrogel-Based Implantable Micromachined Transponder for Wireless Glucose Measurement. *Diabetes Technol. Ther.* **2006**, *8*, 112–122. [CrossRef]
6. Chen, P.J.; Rodger, D.C.; Saati, S.; Humayun, M.S.; Tai, Y.C. Microfabricated Implantable Parylene-Based Wireless Passive Intraocular Pressure Sensors. *J. Microelectromechanical Syst.* **2008**, *17*, 1342–1351. [CrossRef]
7. Ghaed, M.H.; Chen, G.; Razi-ul, H.; Wieckowski, M.; Kim, Y.; Kim, G.; Lee, Y.; Lee, I.; Fick, D.; Kim, D.; et al. Circuits for a Cubic-Millimeter Energy-Autonomous Wireless Intraocular Pressure Monitor. *IEEE Trans. Circuits Syst. I-Regul. Pap.* **2013**, *60*, 3152–3162. [CrossRef]
8. Boutry, C.M.; Beker, L.; Kaizawa, Y.; Vassos, C.; Tran, H.; Hinckley, A.C.; Pfattner, R.; Niu, S.; Li, J.; Claverie, J.; et al. Biodegradable and flexible arterial-pulse sensor for the wireless monitoring of blood flow. *Nat. Biomed. Eng.* **2019**, *3*, 47–57. [CrossRef]
9. Ruth, S.R.A.; Kim, M.G.; Oda, H.; Wang, Z.; Khan, Y.; Chang, J.; Fox, P.M.; Bao, Z.N. Post-surgical wireless monitoring of arterial health progression. *iScience* **2021**, *24*, 103079. [CrossRef]
10. Jiang, H.; Woodhouse, I.; Selvamani, V.; Ma, J.L.; Tang, R.; Goergen, C.J.; Soleimani, T.; Rahimi, R. A Wireless Implantable Passive Intra-Abdominal Pressure Sensing Scheme via Ultrasonic Imaging of a Microfluidic Device. *IEEE Trans. Biomed. Eng.* **2021**, *68*, 747–758. [CrossRef]
11. Lee, H.Y.; Choi, B.; Kim, S.; Kim, S.J.; Bae, W.J.; Kim, S.W. Sensitivity-Enhanced LC Pressure Sensor for Wireless Bladder Pressure Monitoring. *IEEE Sens. J.* **2016**, *16*, 4715–4724. [CrossRef]
12. Behfar, M.H.; Bjorninen, T.; Moradi, E.; Sydanheimo, L.; Ukkonen, L. Biotelemetric Wireless Intracranial Pressure Monitoring: An In Vitro Study. *Int. J. Antennas Propag.* **2015**, *2015*, 918698. [CrossRef]
13. Chen, L.Y.; Tee, B.C.K.; Chortos, A.L.; Schwartz, G.; Tse, V.; Lipomi, D.J.; Wong, H.S.P.; McConnell, M.V.; Bao, Z. Continuous wireless pressure monitoring and mapping with ultra-small passive sensors for health monitoring and critical care. *Nat. Commun.* **2014**, *5*, 5028. [CrossRef] [PubMed]
14. Chiu, Y.; Chen, Y.-Z.; Hsieh, C.-C.; Hong, H.-C. Design and Characterization of a Flexible Relative Pressure Sensor With Embedded Micro Pressure Channel Fabricated by Flexible Printed Circuit Board Technology. *IEEE Sens. J.* **2021**, *21*, 27343–27351. [CrossRef]
15. Li, Y.D.; Zhao, M.; Wei, Q.X.; Yu, J.; Chen, J.; Chen, D.Y.; Wang, J.B. Wireless Passive Intracranial Pressure Sensor Based on Vacuum Packaging. *IEEE Sens. J.* **2020**, *20*, 11247–11255. [CrossRef]
16. Wang, F.; Zhang, X.; Shokoueinejad, M.; Iskandar, B.J.; Medow, J.E.; Webster, J.G. A Novel Intracranial Pressure Readout Circuit for Passive Wireless LC Sensor. *IEEE Trans. Biomed. Circuits Syst.* **2017**, *11*, 1123–1132. [CrossRef]
17. Wei, Q.X.; He, C.C.; Chen, J.; Chen, D.Y.; Wang, J.B. Wireless Passive Intracranial Pressure Sensor Based on a Microfabricated Flexible Capacitor. *IEEE Trans. Electron Devices* **2018**, *65*, 2592–2600. [CrossRef]
18. Ghajar, J. Traumatic brain injury. *Lancet* **2000**, *356*, 923–929. [CrossRef]

19. Lu, D.; Yan, Y.; Deng, Y.; Yang, Q.; Zhao, J.; Seo, M.-H.; Bai, W.; MacEwan, M.R.; Huang, Y.; Ray, W.Z.; et al. Bioresorbable Wireless Sensors as Temporary Implants for In Vivo Measurements of Pressure. *Adv. Funct. Mater.* **2020**, *30*, 2003754. [CrossRef]
20. Kwon, Y.W.; Jun, Y.S.; Park, Y.-G.; Jang, J.; Park, J.-U. Recent advances in electronic devices for monitoring and modulation of brain. *Nano Res.* **2021**, *14*, 3070–3095. [CrossRef]
21. Bratton, S.L.; Chestnut, R.M.; Ghajar, J.; McConnell Hammond, F.F.; Harris, O.A.; Hartl, R.; Manley, G.T.; Nemecek, A.; Newell, D.W.; Rosenthal, G.; et al. Guidelines for the management of severe traumatic brain injury. VII. Intracranial pressure monitoring technology. *J. Neurotrauma* **2007**, *24* (Suppl. S1), S45–S54. [CrossRef] [PubMed]
22. Gong, H.; Xu, Z.; Yang, Y.; Xu, Q.; Li, X.; Cheng, X.; Huang, Y.; Zhang, F.; Zhao, J.; Li, S.; et al. Transparent, stretchable and degradable protein electronic skin for biomechanical energy scavenging and wireless sensing. *Biosens. Bioelectron.* **2020**, *169*, 112567. [CrossRef] [PubMed]
23. Hou, C.; Xu, Z.J.; Qiu, W.; Wu, R.H.; Wang, Y.N.; Xu, Q.C.; Liu, X.Y.; Guo, W.X. A Biodegradable and Stretchable Protein-Based Sensor as Artificial Electronic Skin for Human Motion Detection. *Small* **2019**, *15*, 1805084. [CrossRef] [PubMed]
24. Huang, J.N.; Xu, Z.J.; Qiu, W.; Chen, F.; Meng, Z.H.; Hou, C.; Guo, W.X.; Liu, X.Y. Stretchable and Heat-Resistant Protein-Based Electronic Skin for Human Thermoregulation. *Adv. Funct. Mater.* **2020**, *30*, 1910547. [CrossRef]
25. Wen, H.; Chen, C.; Li, S.; Shi, Y.; Wang, H.; Guo, W.; Liu, X. Array Integration and Far-Field Detection of Biocompatible Wireless LC Pressure Sensors. *Small Methods* **2021**, *5*, 2001055. [CrossRef] [PubMed]